RESEARCH ACTIVITIES II
Department of Molecular Structure

II-A Development of Near-Field Dynamic Spectroscopy and Application to Mesophase Systems

There is much demand for the study of local optical properties of molecular assemblies and materials, to understand mesoscopic phenomena and/or to construct optoelectronic devices in nanometric scale. Near-field optical microscopy, which enables spatial resolution beyond the diffraction limit of light, shows remarkable progress in technology in these days. Combination of this advanced optical technology with ultrafast spectroscopic methods may offer a direct probe of molecular dynamical processes in mesoscopic systems. It may bring essential and basic knowledge for analyzing origins of characteristic features and functionalities of mesophase systems. We are constructing apparatus for near-field dynamic spectroscopy with femtosecond temporal resolution and nanometer spatial resolution. Outlines of the construction and some experimental results are summarized here.

II-A-1 Construction of a Scanning Near-Field Optical Microscope with Closed-Loop Operated Stage and an Apparatus for Fluorescence Life-Time Measurement

IMURA, Kohei; NAGAHARA, Tetsuhiko; OKAMOTO, Hiromi

Scanning near-field optical microscope (SNOM) is the only method that can measure local optical properties beyond the diffraction limit of light. Piezo-electric translator, which is used for sample scanning in SNOM, has a large hysteresis and creeping. Thus, reproducible positioning and stability, which are crucial for investigating local properties in detail, is quite poor. We have developed a SNOM apparatus equipped with closed-loop feedback controlled scanning stage, and achieved about 1 nm positioning accuracy.

The developed instrument consists of light source, sample stage, probe head, distance regulation feedback system, and detection systems. Schematic drawing is depicted in Figure 1. Major mechanical parts of the instrument were made of Super Invar steel to ensure thermal stability. Light source is either a laser or a discharge lamp, the latter is used for absorption spectral measurements. Distance between the probe tip and the sample surface is kept within 10 nm by the shear force feedback control. A polychromator equipped with a CCD array detector is used for spectral measurements while an avalanche photodiode or a photomultiplier tube is used for single photon counting measurements. With this apparatus, we have obtained the lateral resolution down to 50 nm, simultaneously measuring topographic image of the sample.

Time-correlated single photon counting system can be also combined with the SNOM apparatus. It consists of photon detectors, time-to-amplitude converter (TAC), and multi-channel buffer (MCB). From time-correlated photon histograms, fluorescence lifetime can be obtained. Temporal response of the system is determined by the response of the avalanche photodiode, ca. 350 ps.

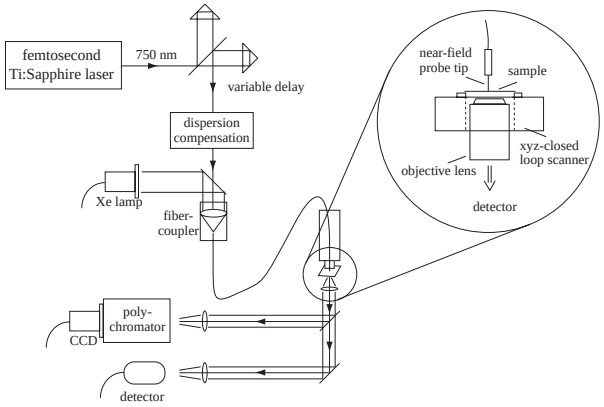

Figure 1. Schematic diagram of experimental set-up. Expansion near the probe is shown at right side.

II-A-2 Near-Field Optical Transmittance Microscopy on the Thin Film of Porphyrin J-Aggregate

NAGAHARA, Tetsuhiko; IMURA, Kohei; OKAMOTO, Hiromi

[*Chem. Phys. Lett.* **381**, 368 (2003)]

Mesoscopic structures and photophysical properties of water-insoluble tetrakis(4-methoxyphenyl)porphyrin (TMeOPP) J-aggregate in thin film have been investigated by illumination (transmission) mode SNOM. In the surface topography (Figure 1A), the TMeOPP J-aggregate sample has been found to be composed of planar microcrystalline structures. In the far-field, a broad strong absorption band centered at 760 nm is seen, whereas a narrower band in the 700–800 nm region and several small peaks are observed in the site-specific near-field spectra (Figure 1B). The differences between the far-field and near-field spectra can be ascribed to spatial inhomogeneities, which is related to the *broad* J-bands.

To analyze further the spatial inhomogeneity, we have assumed that there exists a sharp spectral component, and calculated the correlation between this spectral component and the observed spectra. The mapped

correlation images (Figures 1C and D) show structures that have some correlations with the topography. The finer structures (black arrows) seem to show a tendency to be oriented to the polarization directions, indicating a large transition moment parallel to their long crystalline axes. The results suggest that the assumed sharp spectral component is relevant to a substance that is buried in the inhomogeneously broadened spectrum.

Reference

1) S. Okada and H. Segawa, *J. Am. Chem. Soc.* **125**, 2792–2796 (2003).

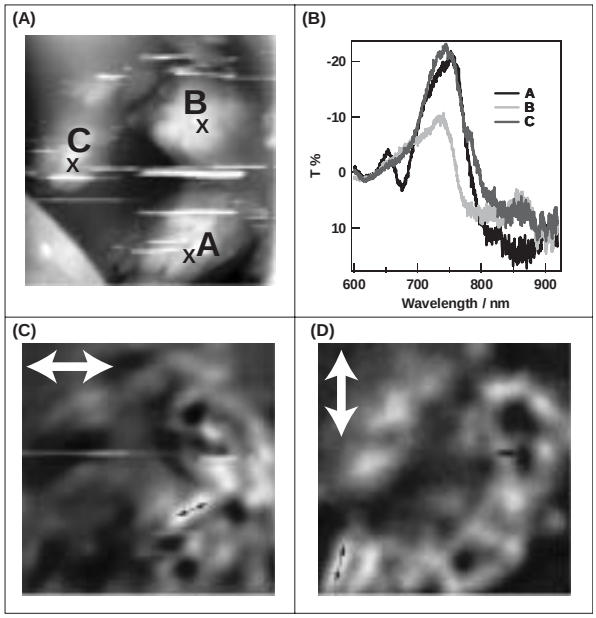

Figure 1. (A) Surface topography of the sample. (B) Transmittance difference spectra in the near-field at positions indicated in (A). (C),(D) Spatial distribution of an assumed spectral component of J-aggregate. Scan range: 5 μm × 5 μm. Arrows in (C) and (D) indicate the directions of the observing polarization.

II-A-3 Time-Resolved Near-Field Spectroscopy of Porphyrin J-Aggregates

NAGAHARA, Tetsuhiko; IMURA, Kohei; OKAMOTO, Hiromi

[*Chem. Phys. Lett.* **381**, 368 (2003)]

We have measured the time-resolved equal-pulse transmission correlation (EPC) of porphyrin (TMeOPP) J-aggregate in the near-field, and tried to elucidate site-specific optical features in mesoscopic scales. In Figure 1B, typical pump-probe EPC signal of TMeOPP observed at position "X" indicated in the topography (Figure 1A) is shown. Time and spatial resolutions, and wavelength of our femtosecond pump-probe SNOM apparatus were 100 fs, 100 nm, and 780 nm, respectively. The observed decay may be ascribed to population decrease in the excited-state. Similar exponential decays are also observed at various positions, but not at a bare glass surface. The lifetimes are raging from 10 to 50 ps, that are of the same order as the reported lifetime (50 ps) of J-aggregate of tetrakis(4-sulfonatophenyl)-porphyrin/H_2O in the far-field, and are distinct from that of monomer (3.87 ns).[1] The scatter of the obtained lifetimes may be ascribed either to site-specificity or experimental errors. Further detailed investigations, to clarify the origin of the variations of the excited-state lifetimes may be needed. More precise lifetime measurements by using moderately lower repetition-rate and higher peak power laser pulses are under way.

Reference

1) N. C. Maiti *et al.*, *J. Phys. Chem.* **99**, 17192–17197 (1995).

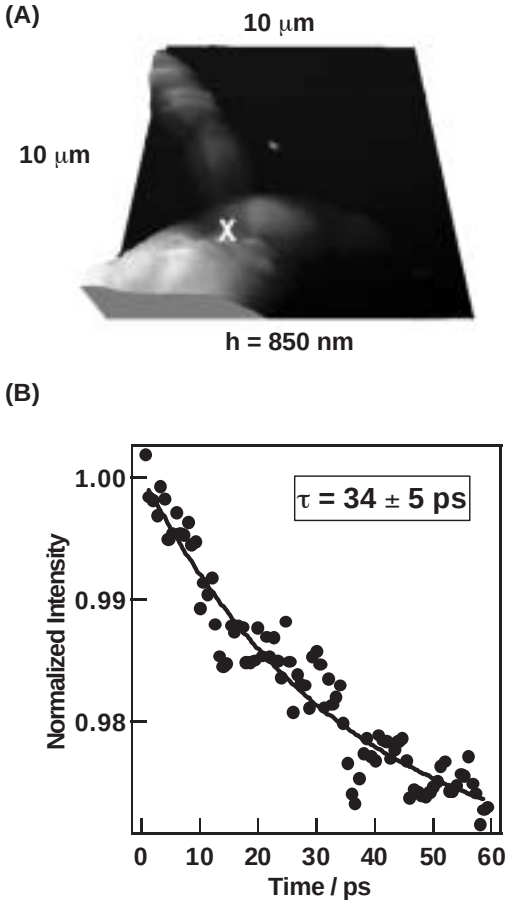

Figure 1. (A) Surface topography of the sample. (B) Equal-pulse transmission correlation signal intensity as a function of delay time, together with that of the least-squares fit.

II-A-4 Near-Field Optical Observation of Gold Nanoparticles

IMURA, Kohei; NAGAHARA, Tetsuhiko; OKAMOTO, Hiromi

For past decades, the surface plasmons (SP) due to collective oscillation of electrons have been widely investigated, for the purpose of understanding physical mechanism in surface enhanced Raman scattering (SERS), and for potential applications in industry as well. Local electric field enhancement near the particle has been recognized as one of the enhancement sources in SERS. Although evidence of local field enhancement has been easily observed after near-field effect translat-

ed into the far-field, little observation in near-field has been reported. In order to understand interaction of photons and the particle in near-field, we have measured near-field transmission spectrum of the particles by a scanning near-field optical microscope (SNOM).

Sample was prepared by spin-coating of 100 nm diameter gold spheres followed by spin-coating with polymer in order to attain flat surface of the sample. Figure 1 shows typical transmission spectrum of a gold particle measured in near-field. Positive and negative signs correspond to enhancement and reduction of the transmission, respectively. We ascribe the enhanced transmission to the antenna effect of the particle. The evanescent wave emerging from the aperture probe first couples into the surface mode of the particle, followed by re-radiation into the far-field. SNOM probe is a source not only of non-propagating evanescent wave but also of propagating wave. Thus, propagating wave also contributes to the observed signal. Absorptive part of the spectrum can be attributed to scattering and absorption, on the gold particle, of the propagating wave from the aperture probe. These considerations imply that spectral profile consists of two different contributions of evanescent and propagating waves.

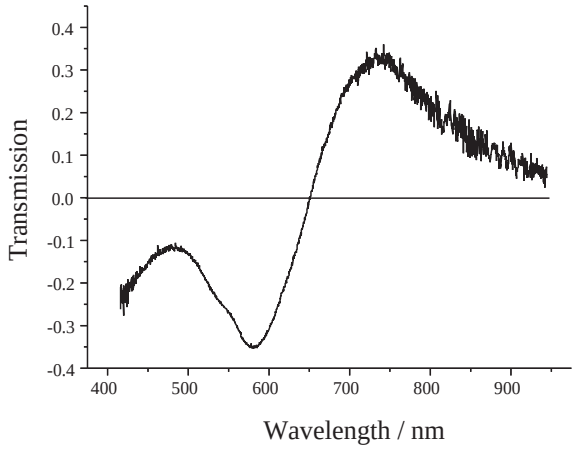

Figure 1. Transmission spectrum of gold sphere (100 nm diameter) measured in near-field.

II-B Laser Cooling and Trapping of Metastable Helium Atoms

In the past two decades, extensive developments have occurred in the laser cooling and trapping of neutral atoms, with many workers reporting the application of these techniques to such diverse atomic species as alkali atoms, alkali earth atoms, and rare gas atoms. Among these, the helium atom is unique on account of its small mass, simple energy level structure, and easy availability in two isotopic forms (^{3}He and ^{4}He) of differing quantum statistics. For this reason, we have been studying the laser cooling and trapping of helium atoms.

II-B-1 Liquid Helium Cooled Metastable Helium Beam Source for Laser Cooling/Trapping Experiments

MORITA, Norio

For laser cooling/trapping of atoms, it is preferable that the initial velocity of an atomic beam is as small as possible, because the higher velocity requires the longer length for stopping the atoms and, therefore, results in the more significant divergence of the beam. For the helium atom, this requirement is more difficult to satisfy, not only because of the small mass, but also because the atoms that can be decelerated and trapped by lasers are only metastable atoms; metastable atoms are, more or less, heated through the excitation procedure, such as discharge. For this reason, metastable helium atoms are, so far, usually produced by discharge in liquid nitrogen cooled circumstances. In the present study, however, we have developed a discharge cell cooled by liquid helium, and investigated the performance of this metastable atomic source. As a result, for ^{4}He, we have found that the metastable beam velocity can be as small as 250 m/s at the peak of the velocity distribution with a width of about 50 m/s, while it is as large as 750 m/s with a liquid nitrogen cooled discharge cell. For ^{3}He, the peak velocity and width are 290 m/s and about 60 m/s, respectively. These results mean that for both ^{4}He and ^{3}He the length enough to stop the atoms is only 15 cm, which is one ninth of the one necessary for stopping metastable atoms produced with a liquid nitrogen cooled source. We can expect that such dramatic shortening of the stopping length will much reduce the difficulty in the cooling/trapping experiments on metastable helium atoms.

II-C Spectroscopic Studies on Atoms and Ions in Liquid Helium

Atoms and ions in liquid helium are known to reside in bubble-like cavities due to the Pauli repulsive force between electrons. Physical properties of these exotic surroundings are determined by the potential energy of the impurity-He$_n$ system, the surface tension energy of the liquid helium, and the pressure-volume work. Spectroscopic studies of such impurity atoms and ions in liquid helium are expected not only to give information on the structure and dynamics of the bubbles but also to contribute to the study on physical properties of superfluid liquid helium.

II-C-1 Laser Spectroscopic Studies of Eu Atoms in Liquid and Solid Helium: Helium Pressure Dependences

MORIWAKI, Yoshiki[1]; MORITA, Norio
([1]Toyama Univ.)

Spectra of Inner shell transitions in Eu atoms distributed in liquid helium have relatively sharp peaks accompanied with long tails of phonon sidebands. The sharp peaks are zero-phonon lines (ZPL), and are largely shifted along with the sidebands, depending on the helium pressure. In this study, we have investigated this pressure shift for both ^{4}He and ^{3}He over a wide pressure range including the solidification region. The pressure shifts of ZPL's in excitation spectra of the inner shell transition $4f^6(^7\mathrm{F})5d6s^2\ ^8\mathrm{F}_{7/2} \leftarrow 4f^7 6s^2\ ^8\mathrm{S}_{7/2}$ at 1.1 K are plotted in Figure 1. As seen in Figure 1, for both ^{4}He and ^{3}He the ZPL is shifted toward longer wavelength at approximately the same rate, which is about 0.06 nm/MPa. For ^{4}He, the ZPL is slightly split above the solidification pressure (2.5 MPa), and two kinds of split pattern are seen, depending, for example, on the procedure of solidification. This might suggest the presence of two crystal structures in solid ^{4}He. Above the solidification pressure, the ZPL wavelength is almost constant and the overall spectral profile keeps unchanged. However, the spectral intensity abruptly increases when the pressure is increased across the solidification pressure. This may indicate that, in solid ^{4}He, Eu atoms are trapped in the solid and cannot freely diffuse. On the contrary, for ^{3}He, neither such abrupt increase of spectral intensity nor the split pattern of the ZPL is observed, while the ZPL wavelength and overall spectral profile keep unchanged above the solidification pressure, just like ^{4}He. This may suggest that, unlike ^{4}He, Eu atoms can move around and diffuse in ^{3}He even in the solid state.

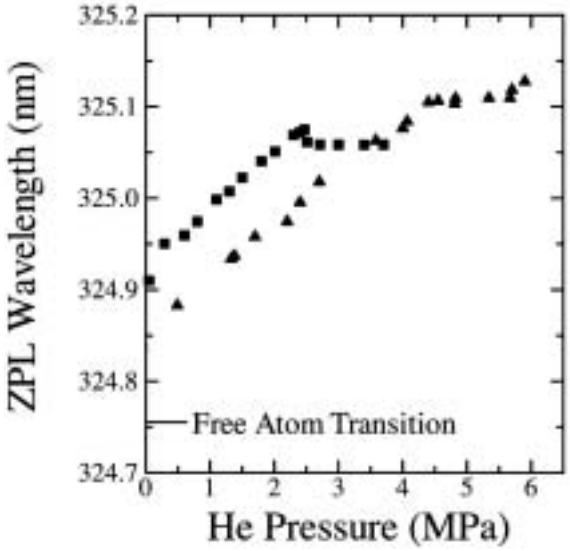

Figure 1. Helium pressure dependence of the wavelength of the zero-phonon line (ZPL) in the excitation spectrum of the $4f^6(^7\mathrm{F})5d6s^2\ ^8\mathrm{F}_{7/2} \leftarrow 4f^76s^2\ ^8\mathrm{S}_{7/2}$ transition of Eu atoms in liquid and solid helium at 1.1 K; ■ represents the ZPL for ^{4}He, and ▲ the one for ^{3}He. At 1.1 K, ^{4}He solidifies at 2.5 MPa, while ^{3}He at 4.3 MPa.

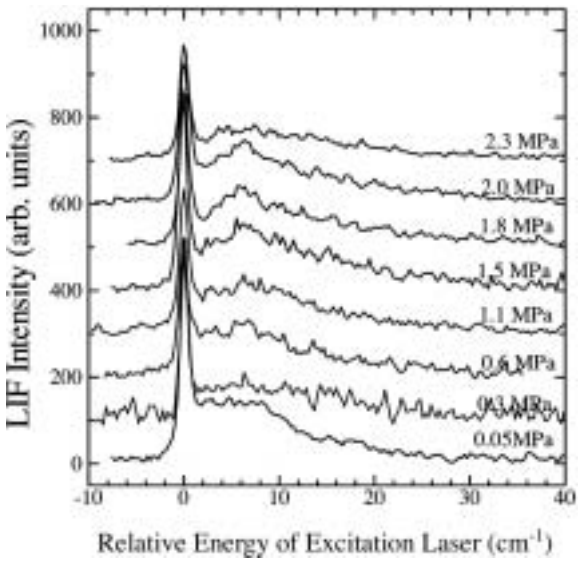

Figure 1. Excitation spectra of the $4f^6(^7\mathrm{F})5d6s^2\ ^8\mathrm{F}_{7/2} \leftarrow 4f^76s^2\ ^8\mathrm{S}_{7/2}$ transition of Eu atoms in liquid ^{4}He at several pressures; the peak shift of the zero-phonon line is ignored for all spectra.

II-C-2 Laser Spectroscopic Studies of Eu Atoms in Liquid ^{4}He: Roton Spectra

MORIWAKI, Yoshiki[1]; MORITA, Norio
([1]Toyama Univ.)

In our previous studies on spectra of the inner shell transition $4f^6(^7\mathrm{F})5d6s^2\ ^8\mathrm{F}_{7/2} \leftarrow 4f76s^2\ ^8\mathrm{S}_{7/2}$ of Eu atoms in liquid ^{4}He, we found some structure of the phonon sideband tail of this transition, and inferred that this structure may be roton spectra because the energy separation between the structure and zero-phonon line roughly agreed to the excitation energy (6 cm^{-1}) of the roton. In order to confirm this inference, in the present study, we have investigated the pressure dependence of the spectra: excitation spectra of this transition at 1.1 K have been measured at several pressures. The results are shown in Figure 1, in which peak shifts of the zero-phonon lines are ignored. In Figure 1, we can find that the peak on the long tail of the phonon sideband is gradually shifted toward lower energy with the increase of the liquid pressure. This characteristic behavior is the same as seen for roton peaks previously observed in two-roton Raman spectra.[1)] This fact strongly supports the inference that the peaks in our spectra are also due to the roton excitation.

Reference

1) K. Ohbayashi *et al.*, *Phys. Rev. B* **58**, 3351 (1998).

II-D Electron Transfer Regulation in Tetraheme Cytochromes *c*

Tetraheme cytochromes *c* are involved in the anaerobic energy metabolism. Cytochrome c_3 (cyt c_3) is an electron transport protein working in strictly anaerobic sulfate-reducing bacteria. This is a small (M.W. ≈ 14,000) soluble protein and shows very low redox potentials (typically, –240 ~ –357 mV *vs.* NHE). We have developed a new expression system using *Shewanella oneidensis*. Using this expression system, now we can examine the role of each amino acid by gene-engineering. At first, we have examined the role of tyrosine-43. We have also determined the complete *g* tensors of the four hemes. Small tetraheme cytochrome *c* (ST cyt *c*) is found in facultative anaerobes of *Shewanella* species and is the smallest tetraheme cytochrome (M.W. ≈ 12,000). The four hemes in ST cyt *c* is arranged in a chain-like manner in contrast to the cyclic heme architecture in cyt c_3. The major aims of this project is to elucidate the mechanism of the regulation of the electron transfer in tetraheme cytochromes *c* on the basis of tertiary structure and heme architecture. For this purpose, we are characterizing two different cytochromes mentioned above by NMR and electrochemistry. Since porphyrin is one of important elemental materials in nano-science, elucidation of the function of particular heme architectures would also contribute to this field.

II-D-1 Role of the Aromatic Ring of Tyr43 in Tetraheme Cytochrome c_3 from *Desulfovibrio vulgaris* Miyazaki F

OZAWA, Kiyoshi[3]; YASUKAWA, Fumiko[3]; TAKAYAMA, Yuki[2]; OHMURA, Tomoaki[4]; CUSANOVICH, Michael A.[5]; TOMIMOTO, Yusuke[6]; OGATA, Hideaki[6]; HIGUCHI, Yoshiki[6]; AKUTSU, Hideo[1]
([1]IMS and Osaka Univ.; [2]Osaka Univ.; [3]Yokohama Natl. Univ.; [4]Mitsubishi Heavy Industries; [5]Unv. Arizona; [6]Kyoto Univ.)

[*Biophys. J.* (2003) in press]

Tyrosine 43 is positioned parallel to the fifth heme axial ligand, His34, of heme 1 in the tetraheme cytochrome c_3. The macroscopic and microscopic formal redox potentials of Y43L and Y43F cytochromes c_3 were determined by differential pulse polarography and ^{1}H-NMR. Although the replacement of tyrosine with leucine increased all the redox potentials, the phenylalanine mutation generally did not change them. This strongly suggests that the aromatic ring at this position contributes to lower the redox potentials of cytochrome c_3. The effect of the leucine and phenylalanine mutations on the interacting potential between heme 1 and heme 2 shows that the aromatic ring is also involved in the cooperative reduction of these hemes. Furthermore, temperature dependent line-width broadening in partially reduced samples established that the aromatic ring at position 43 participates in the control of the kinetics of intramolecular electron exchange. The rate of reduction of Y43L cytochrome c_3 by 5-deazariboflavin semiquinone under partially reduced conditions was significantly different from that of the wild-type in the last stage of the reduction, supporting the involvement of Tyr43 in regulation of reduction kinetics. No significant change was found in the crystal structures of the wild-type and Y43L cytochrome c_3.

II-D-2 Correlation between the *g* Tensors and Nonplanarity of Porphyrin Rings in *Desulfovibrio vulgaris* Miyazaki F Cytochrome c_3 Studied by Single Crystal EPR

SAITOH, Takashi[1]; TACHIBANA, Yoshihiko[2]; HIGUCHI, Yoshiki[3]; HORI, Hiroshi[1]; AKUTSU, Hideo[4]
([1]Osaka Univ.; [2]Yokohama Natl. Univ.; [3]Himeji Inst. Tech.; [4]IMS and Osaka Univ.)

[*Bull. Chem. Soc. Jpn.* in press]

Single crystals of cytochrome c_3 from *Desulfovibrio vulgaris* Miyazaki F are examined by EPR at cryogenic temperature. The principal values and the eigenvectors are determined. The four sets of EPR signals are directly assigned to the specific four hemes in the three-dimensional structure. The relative energy levels of the three *d* orbitals (d_{xy}, d_{xz} and d_{yz}) of each heme iron calculated from the obtained principal *g* values have shown that the energy gap between d_{xy} and d_π is small for a heme with the S_4-ruffled distortion (heme 1 and heme 2) while the energy gap is large for a heme with the S_4-saddled distortion (heme 4). The determined *g* tensor orientations indicated that the principal *g* axes of heme 1, heme 2, heme 3 and heme 4 co-rotate with the imidazole planes of the sixth ligands.

II-D-3 A Directional Electron Transfer Regulator Based on Heme-Chain Architecture in The Small Tetraheme Cytochrome *c* from *Shewanella oneidensis*

HARADA, Erisa[2]; KUMAGAI, Jiro[3]; OZAWA, Kiyoshi[3]; IMABAYASHI, Shinichiro[3]; TSAPIN, Alexandre S.[4]; NEALSON, Kenneth H.[4]; MEYER, Terrance E.[5]; CUSANOVICH, Michael A.[5]; AKUTSU, Hideo[1]
([1]IMS and Osaka Univ.; [2]Osaka Univ.; [3]Yokohama Natl. Univ.; [4]Cal. Inst. Tech.; [5]Unv. Arizona)

[*FEBS. Lett.* **532**, 333–337 (2002)]

The macroscopic and microscopic redox potentials of the four hemes of the small tetraheme cytochrome *c* from *Shewanella oneidensis* were determined. The microscopic redox potentials show that the order of reduction is from hemes in the C-terminal domain (hemes 3 and 4) to the N-terminal domain (heme 1),

demonstrating the polarization of the tetraheme chain during reduction. This makes heme 4 the most efficient electron delivery site. Furthermore, multistep reduction of other redox centers through either heme 4 or heme 3 is shown to be possible. This has provided new insights into the two-electron reduction of the flavin in the homologous flavocytochrome *c*-fumarate reductase.

II-E Surface Chemical Reactions Studied by NEXAFS Spectroscopy

Near edge X-ray absorption fine structure (NEXAFS) is a very promising method to get the quantitative information of surface adsorbed species. Recently, we have developed an energy dispersive NEXAFS method, which is a technique to measure a NEXAFS spectrum in a certain energy range simultaneously. The Hettrick mount monochromator can be used as a polychromator by fully opening the exit slit. Energy dispersed X-rays from the polychromator irradiate the sample surface. Each position of the irradiated surface emits Auger electrons, of which number is proportional to the X-ray absorption coefficient at the corresponding photon energy. By using a position sensitive electron energy analyzer, we can obtain a NEXAFS spectrum from a monolayer-covered surface with a reasonably high signal-to-noise ratio in several tens seconds. This technique has been applied to the study of surface chemical reactions related to fundamental catalytic reactions.

II-E-1 Direct Spectroscopic Observations of the Water Formation Reaction on Pt(111) by NEXAFS and the Simulations with the Kinetic Monte Carlo and the Reaction Diffusion Methods

NAGASAKA, Masanari[1]; KONDOH Hiroshi[1]; AMEMIYA, Kenta[1]; NAMBU, Akira[1]; NAKAI, Ikuyo[1]; SHIMADA, Tohru[1]; OHTA, Toshiaki[2]
([1]Univ. Tokyo; [2]Univ. Tokyo and IMS)

[*J. Chem. Phys.* **119**, 9233 (2003)]

The catalytic water formation reaction was investigated by the energy dispersive NEXAFS spectroscopy. Oxygen covered Pt(111) surface with a (2×2) structure was exposed to gaseous hydrogen (5.0×10^{-9} Torr) at constant surface temperatures (120–140 K). O *K*-edge NEXAFS spectra were measured during the reaction with a time interval of 35 s. From quantitative analyses for the spectra, the coverage changes of the adsorbed species (O, OH, and H_2O) were obtained at 120, 130 and 140 K, as shown in Figure 1. The reaction is composed of three steps, which are characterized by the induction period (I), fast increase in coverage of OH and H_2O with consuming oxygen (II), and slow conversion of OH to H_2O after the consumption of oxygen (III). It was also found that the maximum OH coverage becomes smaller at a higher temperature. The kinetic Monte Carlo simulation has reproduced the three characteristic reaction steps, from which the steps are explained as follows; in the first step OH domains are created through two-dimensional aggregation of H_2O (I), after the nucleation process the second step sets in where the OH domains propagate by the auto-catalytic cycle until they contact with each other (II), and finally the merged OH domains convert to H_2O (III). The Reaction Diffusion simulation has revealed that the density of H_2O nuclei decreases due to its high diffusion rate at a high temperature, which results in reduction of the OH coverage.

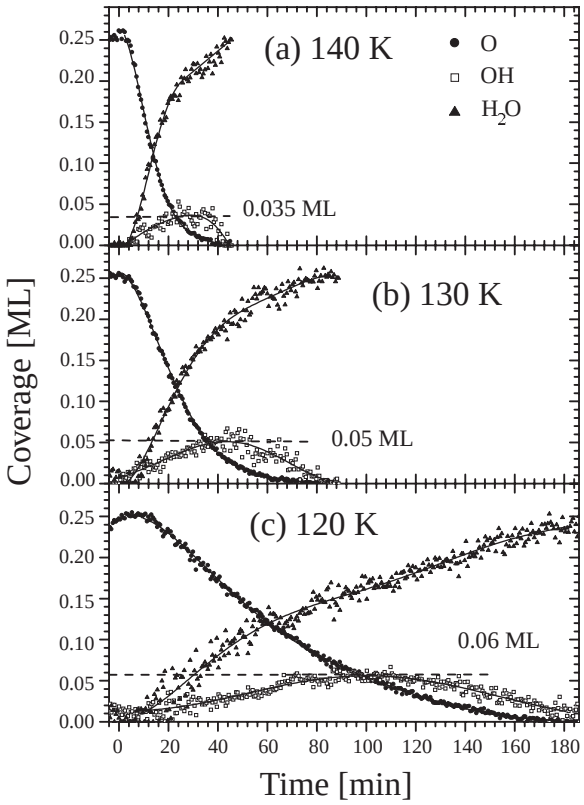

Figure 1. Coverages of O, OH, and H_2O as a function of time during dosing of gaseous H_2 (5.0×10^{-9} Torr) at a surface temperature of (a) 140 K, (b) 130 K, and (c) 120 K. The O-covered Pt(111) surface started exposing to gaseous H_2 at 0 min. The maximum OH coverage was 0.035 ML at 140 K, 0.05 ML at 130 K, and 0.06 ML at 120 K. The reaction finished in 45 minutes at 140 K, 80 minutes at 130 K, and 180 minutes at 120 K.

II-F Ultrafast Dynamics of Surface Adsorbed Species

Understanding of reaction dynamics at surfaces using ultra-short laser techniques is an important issue to clarify the mechanism of the reactions. Real-time observation of temporal change of surface species induced by UV, visible, and (Near-) infrared pump pulses is carried out using mid-IR pump-probe vibrational spectroscopy and Sum-frequency generation (SFG) spectroscopy which is one of the non-linear spectroscopies using ultra-short laser has high sensitivity for detection of molecular vibrations of adsorbed species on surface in the first layer. The aim of this study is the identification of molecular structures of the intermediates generated by electronic, vibrational, or thermal excitation and understanding of the reaction kinetics including potential energies, activation barriers, and entropies. Typical systems of our recent studies are formate (DCOO) adsorbed on Ni(111) surface, CO on OH group of zeolite, and C_6H_6 on Cu(111) surface.

II-F-1 Time-Resolved SFG Study of Formate on Ni(111) Surface under Irradiation of Picosecond Laser Pulses

NOGUCHI, Hidenori[1]; OKADA, Takuya[1]; ONDA, Ken[1]; KANO, Satoru S.[2]; WADA, Akihide[3]; DOMEN, Kazunari[1]
([1]Tokyo Inst. Tech.; [2]Hosei Univ.; [3]IMS and Tokyo Inst. Tech.)

[*Surf. Sci.* **528**, 183–188 (2003)]

Time-resolved sum-frequency generation (TR-SFG) spectroscopy was carried out on a deuterated formate (DCOO) adsorbed on Ni(111) surface to investigate the surface reaction dynamics under instantaneous surface temperature jump induced by the irradiation by pico-second laser pulses. The irradiation of pump pulse (800 nm) caused the rapid intensity decrease of both CD and OCO stretching modes of bridged formate on Ni(111). Different temporal behaviors of intensity recovery between these two vibrational modes were observed, *i.e.*, CD stretching mode recovered faster than OCO. This is the first result to show that the dynamics of adsorbates on metals strongly depends on the observed vibrational mode. From the results of temperature and pump fluence dependence, we concluded that the observed intensity change was not due to the decomposition or desorption, but was induced by a non-thermal process.

II-F-2 Vibrational Relaxation of Adsorbate and Adsorbent in the CO-adsorbed DM-20 Zeolite System

ONDA, Ken[1]; IWASAWA, Yasuhiro[2]; WADA, Akihide[3]
([1]Tokyo Inst. Tech.; [2]Univ. Tokyo; [3]IMS and Tokyo Inst. Tech.)

[*Chem. Phys. Lett.* **370**, 437–442 (2003)]

We made the first observation of transient vibrational spectra of both adsorbate and adsorbent at molecule-adsorbed surface using a two-color infrared picosecond laser system. The transient measurements were carried out on the CO-adsorbed surface hydroxyl group (OD) of DM-20 zeolite by pumping the CO stretching mode (2175 cm^{-1}) or OD stretching mode (2470 cm^{-1}) and probing over the CO and OD stretching region (2000–2700 cm^{-1}). The T_1 lifetime for OD was 5.8 ps and that for CO was 540 ps. By comparison with other CO-adsorbed systems, vibrational relaxation mechanisms of CO on various surfaces are discussed. We also found evidence of energy flows from the vibrational mode of the adsorbent (OD stretching) to that of the adsorbate (CO stretching) *via* van der Waals interaction.

II-F-3 Second Harmonic Observation of Cu(111) Surface: *In Situ* Measurements during Molecular Adsorption

ISHIDA, Hirokazu[1]; MIZOGUCHI, Ryuuichi[1]; ONDA, Ken[1]; HIROSE, Chiaki[1]; KANO, Satoru S.[2]; WADA, Akihide[3]
([1]Tokyo Inst. Tech.; [2]Hosei Univ.; [3]IMS and Tokyo Inst. Tech.)

[*Surf. Sci.* **526**, 201–207 (2003)]

Second harmonic generation (SHG) spectroscopy using a tunable femtosecond laser has been demonstrated as an effective and a practical *in situ* monitor of surface electronic states during adsorption processes. We have successfully shown this technique to be suitable for the study of surface electronic states, not only those induced by adsorbed molecules but also those associated with clean surfaces. By observing the change in the SH signals from a Cu(111) surface during exposure to benzene or CO molecules, we discovered new resonances of the clean Cu surface that could not be ascribed to the well-known surface state (SS)–image state (IS) transition. One of these was from a surface site that is less likely to adsorb benzene, where the SH signal intensity was kept constant until the Cu surface was covered by the sub-monolayer.

II-G Spin Reorientation Transitions of Ultrathin Magnetic Films Induced by Chemisorption

Magnetic anisotropy of ultrathin metal films is one of the most attractive subjects in magnetism. When one considers magnetic anisotropy of thin films within the framework of the classical electromagnetic theory, one finds that in-plane magnetization is always more stable than perpendicular magnetization. Perpendicular magnetic anisotropy (PMA) is, however, sometimes observed in real systems and the understanding of the origin of PMA is important from the viewpoints of both fundamental physics and technological applications to new-generation high-density recording media. We are investigating the microscopic mechanism of PMA that is stabilized by gaseous adsorption on magnetic film surfaces by means of the synchrotron radiation x-ray magnetic circular dichroism (XMCD) and the visible-light magneto-optical Kerr effect (MOKE) techniques. A goal of these works is spin engineering by which the magnetization of ultrathin metal films can be controlled artificially.

II-G-1 Perpendicular Magnetic Anisotropy in Ni/Cu(001) Stablized by Chemisorption of NO

NAKAGAWA, Takeshi; YOKOYAMA, Toshihiko

Spin reorientation transitions (SRT) of ultrathin Ni/Cu(001) films induced by adsorption of nitric oxide (NO) have been investigated by means of MOKE. A wedge-shaped Ni film (4–11 ML) was grown on a clean and ordered Cu(001) surface at room temperature, and was dosed with NO after cooling down to 90 K. The M-H curves were measured using both the polar and longitudinal MOKE geometries. Figure 1 show the observed coersivity (H_c) of the Ni film at 90 K as a function of Ni thickness. On the clean surface H_c abruptly increases at ~ 9 ML, implying that the SRT occurs at this coverage. On the other hand, the NO-adsorbed Ni film shows a clear shift of the SRT coverage at ~ 7 ML. It is concluded that the Ni/Cu(001) film with 7–9 ML thickness exhibits the SRT from in-plane magnetization to perpendicular after NO adsorption. This finding is consistent with the previous works on CO- and H-adsorbed Ni/Cu(001) films.

Let us here compare the coersivity between before and after NO adsorption at the Ni thickness where the SRT does not occur: less than 7 and more than 9 ML. Although the differences are not so large, it is found that in the in-plane magnetized films H_c is suppressed after NO adsorption while H_c is enhanced at the perpendicularly magnetized ones. These results again imply that NO adsorption stabilizes perpendicular magnetization. It is known that the surface magnetic anisotropy constant K_{2s} is negative and favors in-plane magnetization on clean Ni/Cu(001). After NO adsorption, $|K_{2s}|$ is reduced, this leading to the stabilization of perpendicular magnetization, the suppression of H_c for the in-plane magnetization, and the enhancement of H_c for the perpendicular magnetization.

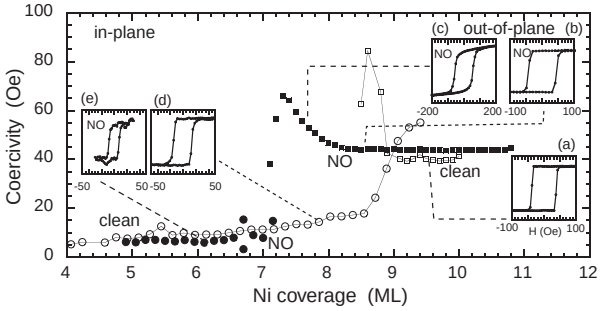

Figure 1. Coersivity of the Ni film at 90 K as a function of Ni thickness before (open circles and squares) and after (filled circles and squares) NO adsorption, obtained by the polar (open and filled squares) and longitudinal (open and filled circles) MOKE measurements. Typical M-H curves are inserted as (a)–(c) (polar) and (d)–(e) (longitudinal).

II-H Local Structures in Photoinduced States of Transition Metal Complexes

Photoinduced phase transition is closely related to bistability of the ground state in the material. Light irradiation stimulates the macroscopic phase transition between the ground state and the metastable state, although thermal fluctuation triggers the thermal phase transition. Although it has been believed that the photoinduced phase is the same state as the thermally induced phase, recent investigations have reported some differences in structure from the high-temperature phase. We have been studying local structures and electronic properties of photoinduced phases of several kinds of transition metal complexes by means of x-ray absorption fine structure (XAFS) spectroscopy. XAFS is one of the most suitable methods for these purposes since the technique does not require long-range order in the sample and provide element-specific information about each metal atom.

II-H-1 Metastable Photoinduced Phase of Cu(II) Ethylenediamine Complexes Studied by X-Ray-Absorption Fine-Structure Spectroscopy

YOKOYAMA, Toshihiko; TAKAHASHI, Kazuyuki[1]; SATO, Osamu[1]
([1]Kanagawa Acad. Sci. Tech.)

[*Phys. Rev. B* **67**, 172104 (4 pages) (2003)]

Recently, a new type of the photoinduced (PI) metastable phase was reported in $Cu(dieten)_2X_2$ (dieten = *N*,*N*-diethylethylenediamine, X = BF_4 and ClO_4) complexes. These materials are known to exhibit thermochromic phase transitions. From the color change the PI transition is expected to be similar to the thermally driven phase transition. The powder X-ray diffraction patterns of the PI phase were, however, found to be different from those of the HT phase, although no correspondence between the structure and diffraction patterns was deduced. In this work, Cu *K*-edge XAFS has been measured and analyzed in order to clarify the molecular structure in the PI phase.

The sample was irradiated by the UV lights (Hg lamp) at 30 K. The Cu *K*-edge near-edge structure indicates that the CuN_4 unit in the PI phase is distorted tetrahedrally, being similar to the HT phase. On the contrary, EXAFS shows a different finding in the second-nearest neighbor Cu–C shells], indicating that the configuration of the surrounding C atoms in the PI phase should be closer to the LT phase rather than to the HT phase.

We can conclude that the PI phase is a new metastable state, whose intramolecular structure is not equivalent to the one of either the HT or LT phase; the CuN_4 unit exhibits tetrahedral distortion, while the atomic configuration of ethylene and ethyl groups is similar to the LT one. One can thus propose a possible model structure shown in Figure 1. The $Cu(dieten)_2$ ion has an inversion center in the LT phase (point group C_i), while it has a C_2 axis in the HT phase (point group C_2). We can suppose that when the LT phase is transformed to the PI phase upon UV irradiation, the CuN_4 plane is distorted tetrahedrally with less reconstruction of the dieten ligand compared to the LT phase. This might be a reasonable hypothesis since the transformation of the configuration of the ethyl groups and also the anions would require too much activation energy to complete at low temperature like 30 K.

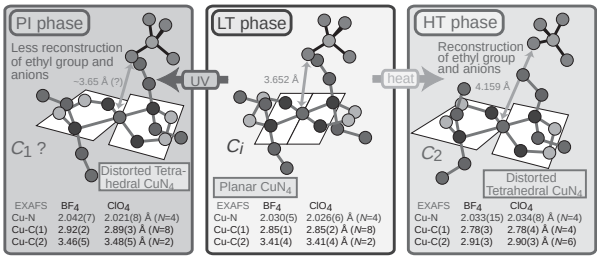

Figure 1. Proposed structure transformation in the PI phase transition.

II-I Molecular and Electronic Structures of Metallofullerenes

The continued interest in radical ions of fullerenes and metallofullerenes has resulted from the discovery of superconductivity in the CT complexes of alkali metals with fullerenes. Spectroscopic information concerning the electronic and spin states of the metallofullerenes has been obtained by ESR measurements.

II-I-1 A Multi-Frequency EPR Study of Endohedral Metallofullerenes Containing the Divalent Eu Ion

MATSUOKA, Hideto; FURUKAWA, Ko; KATO, Tatsuhisa; OZAWA, Norio[1]; KODAMA, Takeshi[1]; NISHIKAWA, Hiroyuki[1]; IKEMOTO, Isao[1]; KIKUCHI, Koichi[1]; SATO, Kazunobu[2]; SHIOMI, Daisuke[2]; TAKUI, Takeji[2]
([1]Tokyo Metropolitan Univ.; [2]Osaka City Univ.)

An endohedral fullerene containing a lanthanoid ion in C_{82} cage, M@C_{82} (M; a lanthanoid ion), has been widely investigated in the field of fullerene science. Our attention in this work has been paid to the metallofullerene containing the divalent Eu ion with the highest spin (S = 7/2) of lanthanoid ion, focusing on the surrounding symmetry of the ion. We isolated three isomers of Eu@C_{82} with the cage structures of C_S, C_2, and C_{2v} symmetry, and Eu@C_{74} with that of D_{3h} symmetry. Their formal electronic structures are represented by $Eu^{2+}@C_n^{2-}$ (n = 74 or 82), where two electrons of Eu atom transfer to the cages. In this work, multi-frequency Electron Paramagnetic Resonance (EPR) measurements were performed to determine their spin-Hamiltonian parameters related to the surrounding symmetry of Eu^{2+} ion. Figure (a) shows W-band EPR spectrum observed for Eu@C_{74} at 4 K. The spin-Hamiltonian parameters were precisely determined by spectral analysis including higher-order zero-field splitting (ZFS) terms. Figures (b) and (c) show the W-band CW-EPR spectra calculated for Eu@C_{74} by using positive and negative D values, respectively. Figure (b) was in good agreement with the observed spectrum, concluding that Eu@C_{74} has the positive D value. A non-zero rhombicity parameter E/D (= 0.11) was obtained for Eu@C_{74}, indicating that Eu(II) ion is not at the center of the C_{74} cage. The spin-Hamiltonian parameters including the signs of the D values for the other sample were also determined in this manner.

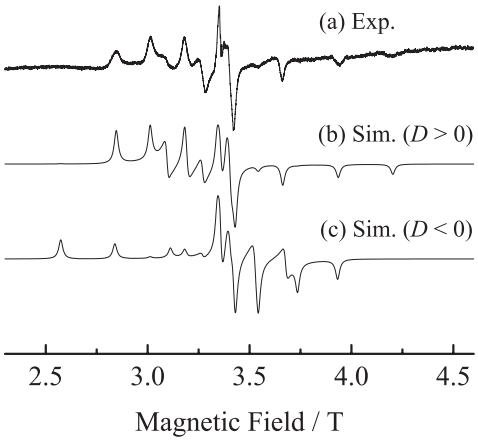

Figure 1. W-band EPR spectra of Eu@C_{74}; (a) experiment; (b) simulation (D > 0); and (c) simulation (D < 0). Experimental conditions: microwave frequency, 95 GHz; temperature, 4 K.

II-I-2 Study on the Electron Spin State of $La_2@C_{80}$ Anion

KATO, Tatsuhisa; MATSUOKA, Hideto; OKUBO, Shingo[1]; DINSE, Klaus-Peter[2]
([1]RIKEN; [2]Darmstadt Tech. Univ.)

An anion form of a lanthanum dimer with C_{80} cage ($La_2@C_{80}^-$) was obtained by chemical and electrochemical reduction. The $La_2@C_{80}^-$ anion exhibited the characteristic Electron Spin Resonance (ESR) pattern for the spin-doublet radical having very large hyper fine coupling (hfc) interaction with the identical two La nuclei, as seen in Figure. The exact values of hfc and g-tensor were determined by ESR measurements with two different frequencies, *i.e.* 9.5 GHz (X-band) and 95 GHz (W-band). The spectrum was completely simulated by parameters shown in Figure. Two La ions were identical, however, they formed a dimer and were fixed at the certain position within the $C_{80}(I_h)$ cage. The total symmetry of $La_2@C_{80}^-$ anion was D_{2h}. The picture of the electronic state was changed from those of a neutral form of $La_2@C_{80}$ by the injection of an excess electron.

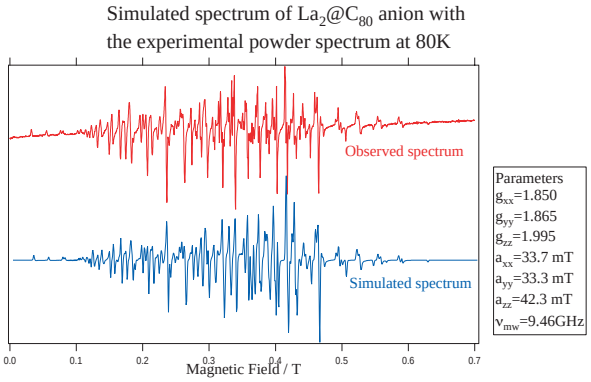

Figure 1. The ESR spectrum of $La_2@C_{80}^-$ anion. The upper spectrum was obtained by a 9.5 GHz (X-band) spectrometer, the lower one was obtained by the simulation using the parameters indicated in the right box.

II-I-3 Spin States of Water-Soluble C_{60} and Metallofullerenes

KATO, Tatsuhisa; MATSUOKA, Hideto; FURUKAWA, Ko; KATO, Haruhito[1]; SHINOHARA, Hisanori[1]; HUSEBO, Lars Olav[2]; WILSON, Lon J.[2]
([1]Nagoya Univ.; [2]Rice Univ.)

Nagoya group of author has shown an application of water-soluble metallofullerens to magnetic resonance imaging (MRI) contrast agents.[1)] It has been found *in vivo* and *in vitro* that water-soluble polyhydroxylated gadolinium metallofullerenols,[2)] $Gd@C_{82}(OH)_n$, exhibit a very strong ability of reducing water proton relaxation times, T_1 and T_2, which results a high MR signal enhancement. This property would be originated from the magnetization due to $4f^7$ radical electrons of Gd^{3+} ion. However, spin states of polyhydroxylated fullerenols have not been clarified in detail. We investigated spin states of $C_{60}(OH)_n$, $La@C_{82}(OH)_n$, $La_2@C_{80}(OH)_n$, and $Gd@C_{82}(OH)_n$ in aqueous solution by using cw-electron spin resonance (cw-ESR) and pulsed-ESR spectrometers. $Gd@C_{82}(OH)_n$ gave a broad cw-EPR spectrum which was characterized by the high spin state of $S = 7/2$, as shown in Figure 1. The other samples in frozen solution showed cw-ESR signal around $g = 4$ as well as $g = 2$. These spectra could be attributed to the spin state of higher spin than $S = 1/2$. Actually the nutation frequency corresponding not only to $S = 1/2$ but also to $S = 1$ was observed by 2D- nutation measurements. $C_{60}(OH)_n$, $La@C_{82}(OH)_n$, and $La_2@C_{80}(OH)_n$ exhibit ESR spectra due to the spin state of $S = 1$, and its magnetization gives the ability of reducing water proton relaxation times in MRI measurement.

References

1) M. Mikawa *et al.*, *Bioconjugate Chem.* **12**, 510–514 (2001).
2) H. Kato *et al.*, *Chem. Phys. Lett.* **324**, 255–259 (2000).

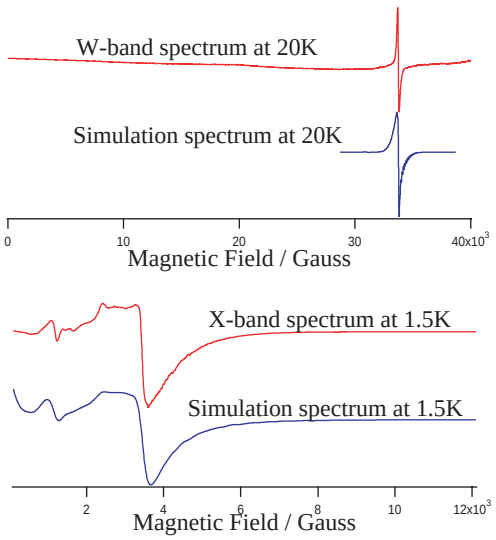

Figure 1. EPR spectra of $Gd@C_{82}(OH)_n$ obtained by a 9.5 GHz(X-band) spectrometer, the lower trace, and by a 95 GHz (W-band) one, the upper trace.

II-I-4 Chemical Reactivity and Redox Property of $Sc_3@C_{82}$

KATO, Tatsuhisa; KOBAYASHI, Kaoru; NAGASE, Shigeru; WAKAHARA, Takatsugu[1]; IIDUKA, Yuko[1]; SAKURABA, Akihiro[2]; OKAMURA, Mutsuo[2]; TSUCHIYA, Takahiro[1]; MAEDA, Yutaka[1]; ISHIZUKA, Midori O.[1]; AKASAKA, Takeshi[1]; KADISH, Karl M.[3]

([1]Univ. Tukuba; [2]Niigata Univ.; [3]Univ. Houston)

The photochemical and thermal reactions of $Sc_3@C_{82}$ with disilrane afforded an exohedral adduct indicating the high reactivity of $Sc_3@C_{82}$. The redox potentials of $Sc_3@C_{82}$ in *o*-dichlorobenzene show a high electron affinity and a small band gap. The $Sc_3@C_{82}$ anion was prepared by electrochemical reduction, which possesses a diamagnetic character. Recently, we have accomplished the chemical reduction of endohedral metallofullerenes as $La@C_{82}$ and $La_2@C_{80}$ in the pyridine and DMF solution. In this context, $Sc_3@C_{82}$ may exist as an anionic form in pyridine. No ESR signal was observed at room temperature in the ESR spectrum of $Sc_3@C_{82}$ in the presence of pyridine, indicating the formation of the diamagnetic $Sc_3@C_{82}$ anion (Figure 1). After removal of pyridine, the residue was resolved again in toluene. Interestingly, the ESR spectrum of $Sc_3@C_{82}$ was recovered, and it was accompanied by a triplet spectrum at $g = 2.0403$, as can be seen in Figure 1. The recovered spectrum was identical with the original $Sc_3@C_{82}$ one in terms of *g*-value, 1.9985, and isotropic hfs constant, 6.25 gauss. The accompanying triplet splitting would come from the hfs of ^{14}N nucleus, which would be due to a by-product of chemical reduction by pyridine. These observations surely reveal that $Sc_3@C_{82}$ can exist as an anionic form in pyridine.

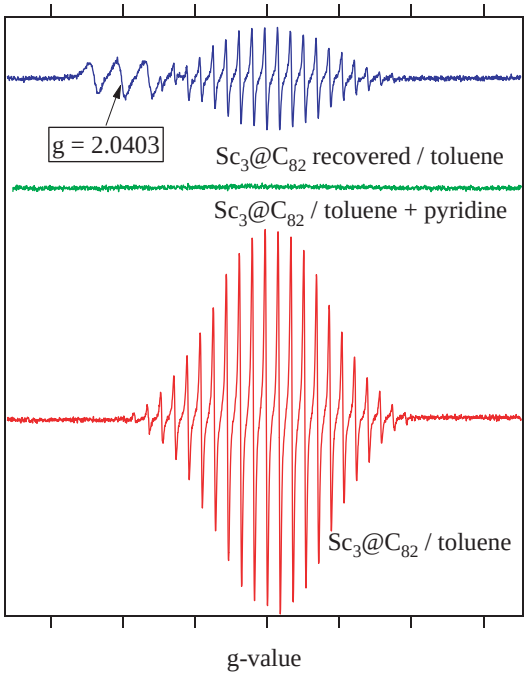

Figure 1. Twenty two lines of ESR spectrum of $Sc_3@C_{82}$ in toluene, the lower trace, disappeared in the presence of pyridine as shown in the middle trace, indicating the formation of the diamagnetic $Sc_3@C_{82}$ anion. After removal of pyridine, the residue was resolved again in toluene and exhibited the ESR spectrum of $Sc_3@C_{82}$. It was accompanied by a triplet spectrum at $g = 2.0403$. The recovered spectrum was identical with the original $Sc_3@C_{82}$ one in terms of *g*-value, 1.9985, and isotropic hfs constant, 6.25 gauss.

II-I-5 Hyperfine Interactions in La@C_{82} Studied by W-Band EPR and ENDOR

KATO, Tatsuhisa; WEIDEN, Norbert[1]; DINSE, Klaus-Peter[1]
([1]Darmstadt Tech. Univ.)

The analysis of dipolar and quadrupolar lanthanum hyperfine data measured with EPR and ENDOR reveals that at low temperatures no significant change occurs at the internal binding site of the endohedral complex. We interpret this result as indicative of freezing of the large-scale motion of the encased ion, which is observed at room temperature. Averaging of hyperfine interactions is fast on the time scale of the EPR experiment, prevening drastic changes of dipolar and quadrupolar hfi, providing that the equilibrium position is unchanged. The detection of hyperfine interaction in disordered samples was possible by invoking orientation selection in the 94 GHz EPR spectrum. Quadrupolar hfi could be directly measured for the first time in a metallo-endohedral fullerene complex.

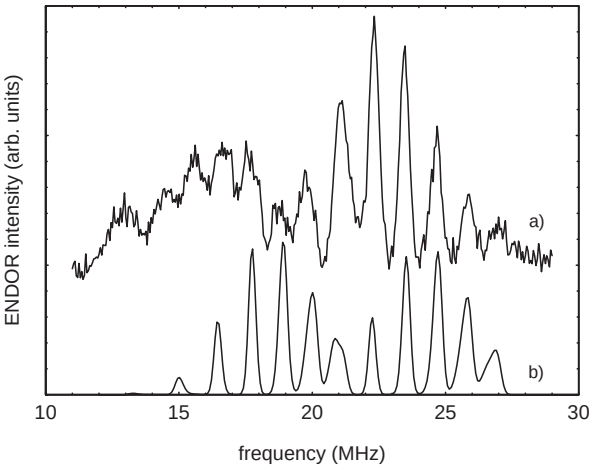

Figure 1. a) W-band pulsed ENDOR spectrum of La@C_{82}(I) measured at 10 K at B_0 = 3371.6 mT. The spectrum was accumulated when exciting the high-field edge of the EPR spectrum and by invoking a Davies pulse sequence. b) A simulated spectrum used to identify the individual line positions is also shown.

II-J High Field and Pulsed Electron Spin Resonance Spectroscopy

Electron paramagnetic resonance (EPR) spectroscopy has been a powerful technique for the characterization of radical species. The modern development of EPR spectroscopy enables us to investigate the heterogeneous and disordered system in detail. Especially the high frequency and pulsed EPR methods achieve the substantial resolution enhancement of spectrum. The advanced EPR spectroscopy is applied to study on the spin state in the heterogeneous system.

II-J-1 A Discrete Self-Assembled Metal Array in Artificial DNA

KATO, Tatsuhisa; TOYAMA, Namiki; TANAKA, Kentaro[1]; TENGEIJI, Atsushi[1]; SHIONOYA, Mitsuhiko[1]
([1]Univ. Tokyo)

[*Science* **299**, 1212–1213 (2003)]

DNA has a structural basis to array functionalized building blocks. Here we report the synthesis of a series of artificial oligonucleotides, d(5'-GH_nC-3') (n = 1 to 5), with hydroxypyridone nucleobases (H) as flat bidentate ligands. Righthanded double helices of the oligonucleotides, $n$$Cu^{2+}$ d(5'-GH_nC-3')$_2$ (n = 1 to 5), were quantitatively formed through copper ion (Cu^{2+}) –mediated alternative base pairing (H–Cu^{2+}–H), where the Cu^{2+} ions incorporated into each complex were aligned along the helix axes inside the duplexes with the Cu^{2+}–Cu^{2+} distance of 3.7 ± 0.1 angstroms. The Cu^{2+} ions were coupled ferromagnetically with one another through unpaired *d* electrons to form magnetic chains. Continuous-wave electron paramagnetic resonance (CW-EPR) spectra of the duplexes Cu-n (n = **1**–**5**) in a frozen aqueous solution were recorded at 1.5 K by a conventional X-band spectrometer (Figure 1). The spectrum of the mononuclear complex Cu-**1** was reproducible in a simulation as arising from a doublet (S = 1/2) radical of a Cu^{2+} center in the square-planar ligand field. However, spectra of Cu-**2**, Cu-**3**, Cu-**4**, and Cu-**5** exhibited quite different patterns from that of Cu-**1**. The spectrum of Cu-**2** could be attributed to the spin state of S = 1, that of Cu-**3** to S = 3/2, and those of Cu-**4** and Cu-**5** to S = 2 and S = 5/2, respectively. The results obtained by CW-ESR spectra were confirmed by the Transient Nutation measurement of a pulsed-ESR. With accumulating Cu^{2+} ions, the electron spins on adjacent Cu^{2+} centers are aligned parallel and couple in a ferromagnetic manner, with Cu-n (n = **1**–**5**) attaining the highest spin state, as expected from a lineup of n Cu^{2+} ions.

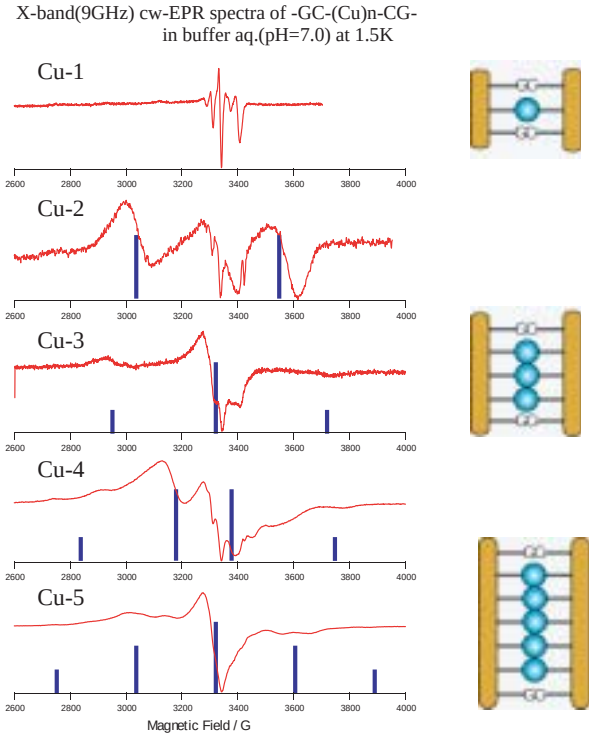

Figure 1. CW-EPR spectra of the duplexes Cu-*n* (*n* = **1**–**5**) in frozen aqueous solution at 1.5 K, recorded by an X-band spectrometer with a 9.5-GHz microwave.

II-J-2 Charge Transport in the Insulating State of (DMe-DCNQI)$_2$Li above T_{SP}: A Possible Fractional Charge Soliton Conduction with $\pm\frac{1}{2}e$

KATO, Tatsuhisa; HIRAOKA, Maki[1]; SAKAMOTO, Hirokazu[1]; MIZOKUCHI, Kenji[1]; KATO, Reizo[2]
([1]Tokyo Metropolitan Univ.; [2]RIKEN)

[*Phys. Rev. Lett.* **91**, 056604 (2003)]

A spin-Peierls system (DMe-DCNQI)$_2$Li is studied with *W*-band electron paramagnetic resonance (EPR) (94 GHz) to unveil a charge transport mechanism in the insulating $4k_F$ charge density wave state above T_{SP}. The electron hopping between the neighbor DCNQI columns provides an additional broadening of the EPR linewidth, since the neighbor columns are generally nonequivalent to each other with respect to *g* shift. The obtained intercolumn hopping rates lead us to the conclusion that the electron hopping to a hole soliton carrying a fractional charge of *e*/2 in the neighbor column dominates the intercolumn charge transport.

II-J-3 Magnetic Properties for Hexaphyrin

FURUKAWA, Ko; KATO, Tatsuhisa; VENKATARAMANARAO, G. Arnand[1]; SHIMIZU, Soji[1]; ARATANI, Naoki[1]; OSUKA, Atsuhiro[1]
([1]Kyoto Univ.)

Magnetic properties for the hexaphyrin **1** with the Cl and O bridging ligands, the hexaphyrin **2** without the bridging ligand, and the hexaphyrin **3** with the O bridging ligand (see Figure 1) were examined. In these hexaphyrins **1**–**3**, not the direct exchange coupling between the Cu ions but the superexchange coupling *via* the bridging ligands is expected due to the much long Cu–Cu distance. These systems are the attractive materials from the viewpoint of the superexchange interaction.

Figure 1 shows the temperature dependence of the χ_pT values for **1**–**3**. The observed values were reproduced by the typical spin hamiltonian $H = -2J\mathbf{S}_i\cdot\mathbf{S}_j$, where *J* denotes the exchange coupling parameters (J/k_B = –17.3 K for **1**, J/k_B = –230 K for **3**). The χ_pT values for **2** are independent of the temperature. The spin structures for both hexaphyrins **1** and **3** have the singlet ground states. The remarkable points are the following two; (1) the exchange coupling for both **1** and **3** is antiferromagnetic, although the superexchange interaction should be ferromagnetic according to the Goodenough-Kanamori-Anderson (GKA) rule[1)] and (2) the J/k_B value for **3** is much larger than that for **1**.

The GKA rule is assumed that the *d* orbital for the metal ions and the degenerated *p* orbitals for the bridging ligand take part in the superexchange interaction. The antiferromagnetic superexchange interaction is induced by the breakdown of the degeneracy of the *p* orbitals, which is caused by the chemical bond between the ligand O and the C atom on the hexaphyrin ring. In the hexaphyrin **1**, the superexchange interaction for the Cu–Cl–Cu pathway becomes ferromagnetic because of the equivalency between the *p* orbitals of the ligand Cl. Totally, the exchange coupling in **1** is weaker than that for **3**.

Reference

1) J. Goodenough, *Magnetism and the Chemical Bond*, John Wiley and Sons; New York (1963).

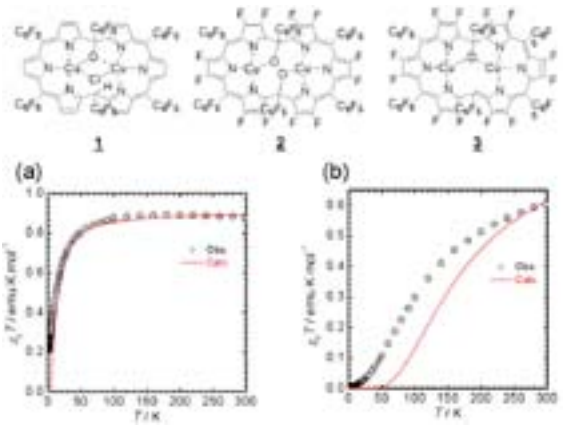

Figure 1. Temperature dependence of the χ_pT values for hexaphyrin (a)**1**, (b)**3**. The circles and lines stand for the observed and calculated values.

II-J-4 Determination of Spin State and Observation of ESEEM for Di- and Tri-Cation of Oligoanilines

KATO, Tatsuhisa; HIRAO, Yasukazu[1]; ITO, Akihiro[1]; TANAKA, Kazuyoshi[1]

([1]Kyoto Univ.)

The ESR spectroscopy showed that high-spin species were generated by chemical oxidation of N,N,N',N',N",N"-Hexakis[4-(di-4-anisylamino)-phenyl]-1,3,5- benzenetriamine in solution. The polycationic species formed by two equivalent of oxidant was assigned to be the triplet spin state, and that by three equivalent of oxidant to be the quartet spin state, respectively, on the basis of ESR spectroscopy. The assignment was confirmed by the 2 dimensional nutation (2D Nuation) measurement of pulsed ESR spectroscopy. Each polycation exhibited the specific ESEEM (Electron Spin Echo Envelope Modulation) frequency in 2-pulsed and 3-pulsed echo-decay measurement. And they gave the auto-correlation peak at the frequency associated with ESEEM in the two dimensional spectrum obtained by the HYSCORE (hyperfine sublevel correlation spectroscopy) sequence.

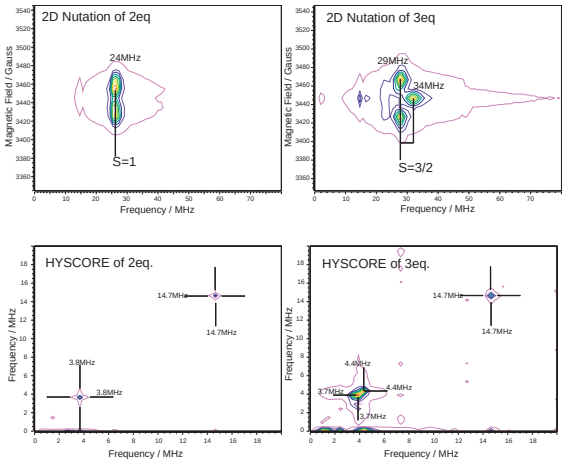

Figure. 1 The upper two contour maps are 2D Nutation spectra for the di-cation and the tri-cation. The lower two contour maps are HYSCORE spectra for the di-cation and the tri-cation.

II-K State Correlated Raman Spectroscopy

The vibrational Raman polarizability tensor responds to molecular reorientational relaxation process, and the structural environment in condensed media. The measurement of Raman scattering is a powerful technique for the investigations of molecular structure, molecular motion, and the mechanism of phase transition. We've built up the system of multichannel type detection of Raman scattering combined with the temperature controlled cell.

II-K-1 Intrinsic Aspect of V-Shaped Switching in Ferroelectric Liquid Crystals: Biaxial Anchoring Arising from Peculiar Short Axis Biasing in the Molecular Rotation around the Long Axis

HAYASHI, Naoki; KATO, Tatsuhisa; ANDO, Tomohiro[1]; FUKUDA, Atsuo[2]; KAWADA, Sachiko[3]; KONDOH, Shinya[3]
([1]Shinshu Univ.; [2]Univ. Dublin; [3]Citizen Watch Co., Ltd.)

[*Phys. Rev. E* **68**, 11702 (2003)]

To clarify the intrinsic aspect of practically usable thresholdless V-shaped switching in ferroelectric liquid crystals, we have observed textures and measured polarized Raman scattering as well as optical transmittance in a thin homogeneous cell of a single compound by applying an electric field. The results indicate that the so-called surface stabilized ferroelectric states are destabilized, and that there exist rather stable two domains [Figure 1(a)] with broad and narrow molecular orientational distributions, both of which show the almost ideal V-shaped switching with considerably low transmittance at the tip of the V [Figure 1(b)]. We have concluded that the main cause of the V-shaped switching is the biaxial anchoring on the substrates coated with polyimide, which makes the most polarizable short axis normal to the substrates. It is in a competition with the ordinary anchoring that favors the director parallel to the substrates, when the material has such a bulk intrinsic property that this short axis is parallel to the tilt plane. The competition makes the total anchoring energy almost independent of the azimuthal angle and gives rise to the V-shaped switching.

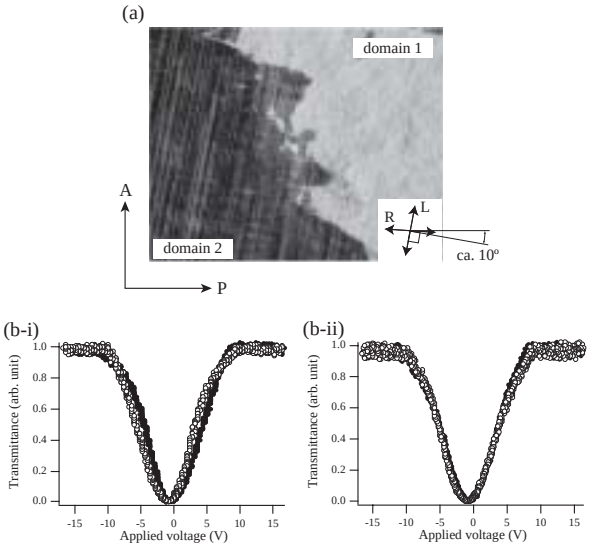

Figure 1. (a) Optical micrographs of textures taken after the long-term switching. The arrow "L" indicates the layer direction and the arrow "R" indicates the rubbing direction.

(b) Electro-optic responses observed in domains 1 [(b-i)] and 2 [(b-ii)]. Solid and open circles were obtained by increasing and decreasing the applied electric field, respectively.

II-K-2 A Large Tilt in the Core Relative to the Molecular Rotational Long Axis as Observed by Polarized Raman Scattering in a de Vries Smectic-*A* Liquid Crystal

HAYASHI, Naoki; KATO, Tatsuhisa; FUKUDA, Atsuo[1]; PANARIN, Yuri P.[1]; VIJ, Jagdish K.[1]; NACRI, J.[2]; SHASHIDHAR, R.[2]; KAWADA, Sachiko[3]; KONDOH, Shinya[3]
([1]Univ. Dublin; [2]Naval Research Laborator; [3]Citizen Watch Co., Ltd.)

The second- and fourth-order orientational order parameters of the core part of the molecule, $\langle P_2 \rangle$ and $\langle P_4 \rangle$, have been measured by polarized vibrational Raman spectroscopy for a homogeneously aligned ferroelectric smectic liquid crystal with three dimethyl siloxane groups in the achiral alkyl terminal chain, which shows the de Vries-type phenomena; very large electroclinic effect in the smectic-*A* (Sm-*A*) phase and a negligible layer contraction at the phase transition between the Sm-*A* and Sm-*C** phases. The orientational order parameters of the rigid core part of the molecule are extremely small both with and without the external electric field in Sm-*A*; $\langle P_4 \rangle$ is only approximately 0.1 while the apparent tilt angle reaches at 32º when a sufficiently high electric field is applied to the cell. This result indicates that the core part is tilted by 26–36º relative to the molecular rotational long axis (Figure 1).

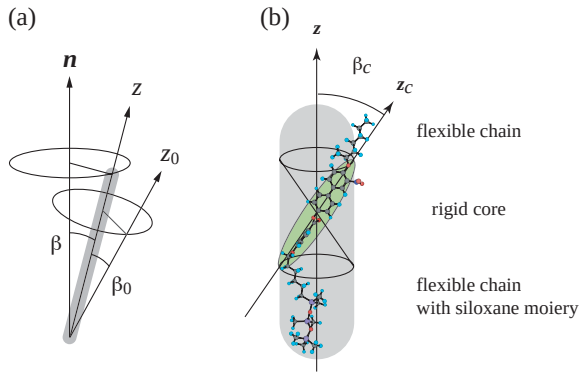

Figure 1. Schematic illustrations representing (a) the molecular rotational long axis (the *z* axis), the averaged direction of the molecular rotational long axes (the in-layer director, ***n***), and the longest principal axis of the Raman tensor (the z_0 axis), and (b) the molecular rotational long axis (the *z* axis) and the long axis of the core part (the z_c axis). Here β is the molecular tilt angle at an instant of time, β_0 the angle between the *z* and z_0 axes, and β_c the angle between the *z* and z_c axes. The molecules are rotating freely around their long axes, of which the distribution around the in-layer director is uniaxial. The z_c and z_0 axes are almost parallel each other and hence we assume $\beta_0 = \beta_c$. The conformation of the chemical structure illustrated is not a real one but is drawn just for the ease of understanding.